Shock Waves (2010) 20:29–40
DOI 10.1007/s00193-009-0237-3

ORIGINAL ARTICLE

Experimental investigation on the shock-wave load attenuation by geometrical means

Shachar Berger · Oren Sadot · Gabi Ben-Dor

Received: 15 March 2009 / Revised: 22 September 2009 / Accepted: 7 October 2009 / Published online: 11 November 2009

Abstract The pressures and loads induced on the center of the end-wall of a shock tube by a shock wave that passes through different types of obstacles are investigated. Efforts have been made to understand the effect of the obstacle geometry on the load development. The experiments were conducted in a shock tube apparatus in which a modular test section was implemented. It is found that for a single-obstacle setup, the effect of the geometry becomes dominant when the blockage ratio (i.e., the ratio of the non-open area to the overall cross section) is large. It is also found that the attenuation effect is more pronounced for general geometries, which form diverging-like nozzle. In the case of multi-obstacles geometry, the same sensitivity to the blockage ratio as in the single-obstacle case is found. However, amplification or attenuation of the shock-wave load on the center of the end-wall of a shock tube is observed when the number of the obstacles is increased. This is due to different trapping effects of the shock wave between the obstacle and the end-wall.

Keywords Shock wave attenuation · Shock wave mitigation · Shock tube · Shock trapping · High-speed photography

PACS 47.40.Nm

Communicated by B.W. Skews.

S. Berger · O. Sadot (✉) · G. Ben-Dor
Department of Mechanical Engineering,
Faculty of Engineering Sciences,
Pearlstone Center for Aeronautical Engineering Studies,
Protective Technologies R&D Center,
Ben-Gurion University of the Negev,
POB 653, 84105 Beersheba, Israel
e-mail: sorens@bgu.ac.il

1 Introduction

Attenuation of shock-wave loads by geometrical means is of great importance in many engineering applications. The interaction between shock waves and rigid obstacles or orifice plates, modifies considerably the flow field by introducing new waves (shocks, compressions and rarefaction), vortices, and regions of intense turbulence. These new waves can reduce the energy traveled with the transmitted shock wave and the load imposed by it.

Although experimental investigations of this subject appeared first in the early 1950s, little research has been done to investigate and explore these effects. In pioneering experimental work by Dosanjh [1], shadowgraph photography was exploited to investigate the wave pattern that resulted from the head-on collision of an incident shock wave with a grid like obstacle. Dosanjh [1] was the first to observe and explain the chocking phenomenon in the supersonic flow immediately behind the obstacle. The idea of choking the flow in order to reduce the load downstream was introduced later by Lind et al. [2]. Franks [3] used schlieren- and interferometer-based optical systems to record the wave pattern generated following the interaction of a shock with a grid. He also observed the choking effect and introduced an analytical model to describe the flow. His model was based on the assumption that the flow underwent an isentropic expansion. Britan et al. [4] investigated recently the attenuation of a shock wave by grid and orifice plates. In their work, the interaction of weak shock waves with porous barriers of different geometries and porosities was examined. The barrier inside the test section of a shock tube initiated the development of a complex wave pattern following the interaction between the incident shock wave and the barrier. They proposed a one-dimensional (1D), inviscid flow model for predicting the flow that results from the collision of an incident shock

wave with the barrier. In their study, they found that the peak pressure at the center of the end-wall was reduced almost linearly with the distance between the grid-like barrier and the end-wall. The flow developed between the barrier and the end-wall was approximated using a 1D, inviscid flow model. It was shown that good agreement existed between the measured and the predicted findings based on this 1D model. The shock-wave load could be reduced by forcing abrupt changes in its direction of propagation, as in a bent duct [5] by passing through particle suspensions [6–8], or passing through perforated tube linings [9]. All of these measures were suggested as mechanisms by which a shock wave emerging from a duct or tube can be mitigated. Another suggested concept was to use different types of energy absorption layers in front of the target that was to be protected against shock-wave loads. Different ideas were introduced, i.e., liquid [10], plastics [11] and even metallic foams [12]. However, this type of protection could not be implemented in many applications.

Schardin and Reichenbach [13] tested the effect of wall roughness on shock wave attenuation. In their study, the shock tube was divided into three channels where in each of them a different surface roughness size was imposed by means of coating the surface with abrasive power of appropriate granulation. The shock velocities over the different geometries were measured by optical means and it was found that by increasing the surface roughness the attenuation of the shock wave increased. Sasoh et al. [9] conducted experimental and numerical studies on pseudo-perforated walls. They found that due to complex interactions of the incident shock wave with the perforated walls, the overpressure behind the transmitted shock became non-uniform and the peak values could locally exceed the value behind the undisturbed incident shock wave. However, the pressure gradient monotonically decreased as the shock wave propagated. They concluded that for a shock wave generated at the outlet of a train tunnel, the perforated wall solution was effective if the pseudo-perforation section was sufficiently long. Abe and Takayama [14] investigated the attenuation of shock waves propagating over complex geometries. In their study, shock wave attenuation by an array of spheres and cylinders were visualized quantitatively by sequential holographic interferometry. It was revealed that for identical initial conditions and blockage ratio, shock waves attenuate faster in the case of arrayed spheres than arrayed cylinders. Moreover, the shock wave attenuation was found not to be proportional to the blockage ratio.

In the present experimental investigation, we focused on the effect of large obstacles on the shock-wave load developed at the center of the end-wall of a shock tube. The effect of the geometry of the obstacle was investigated. In contrast to grid-like obstacles where the choking effect was found to play a major roll in many obstacle geometries, no such effect was observed in the present investigation. For better understanding the effect of the geometry of the obstacle on the flow, a progressive investigation was conducted. At the first stage, single-obstacles with different geometries were implemented and their effect on the load developed at the center of the end-wall was studied. At the second stage, the effect of the number of obstacles was investigated. The experimental system will be presented in Sect. 2; the results in Sect. 3; and the conclusions in Sect. 4.

2 Experimental apparatuses

The experimental investigation was conducted in a shock tube facility at the Shock Tubes Laboratory of the Protective Technologies R&D Center of the Ben-Gurion University. The shock tube that was used was horizontal, 5.5-m long, with an internal cross-section of 8 cm × 8 cm. Shock waves of moderately low Mach numbers $M_s = 1.2$ were generated in it. The shock wave was generated by rupturing a mylar diaphragm, by means of a striking pin, that initially separated the driven section from the driver section that was pressurized to the required initial pressure. The shock wave interacted with the obstacles that were placed in the test section. Pressure histories of the flow in the shock tube were obtained using at least three piezoelectric pressure transducers. The pressure history diagnostic system was based on ENDEVCO piezoresistive pressure gages (model 8510B-500) and electric ENDEVCO amplifier (model 136). The pressure signals after being converted to electric signals by the amplifier were captured by a LeCroy (model LT344 WaveSurfer) digital oscilloscope.

Transparent plexi-glass side-wall windows were installed in the test-section of the shock tube in order to allow flow visualization. The evolution of the shock-obstacles interaction was documented by a set of schlieren photographs obtained for each experiment, using a pulsed frequency-doubled Nd^{3+}:YAG laser (532 nm) as the light source and a shutterless high-speed rotating drum camera. The laser produced 240 ns-long pulses with a repetition rate up to 50 kHz and energy of approximately 2.4 mJ per pulse. The photographs were captured on a 35 mm black/white KODAK photography film (T-Max 400 *ASA*). The photography film was digitized using a film scanner. The photographs were analyzed using an in-house computerized image analysis software platform that was based on MATLAB®.

Figure 1 presents a schematic drawing of the experimental apparatus. The synchronization between the shock wave, laser light and the data acquisition system were done using a National Instruments PCI programmable card (NI-6602) and an in-house developed code using the LabView software.

The diaphragm initially separating the driver section from the driven section was ruptured at the desired instant by an electrically actuated striking pin mounted on a rod inside the driver section. This procedure ensured a ±1% variation in

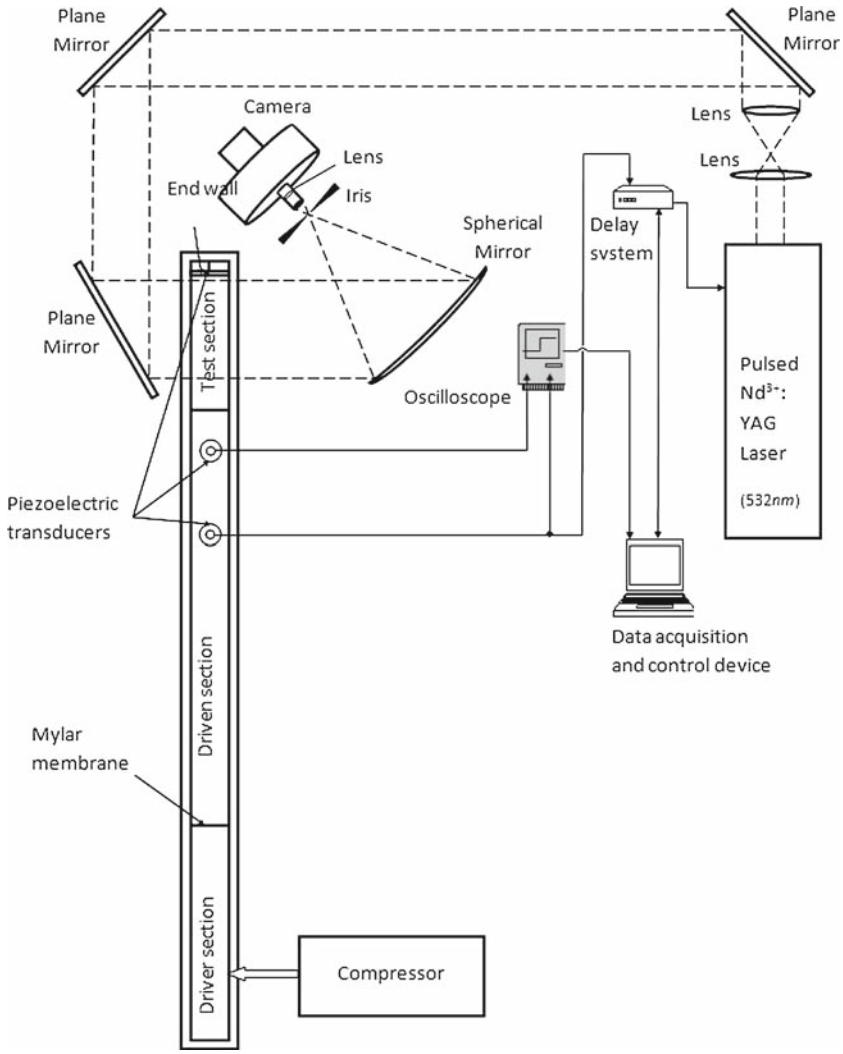

Fig. 1 Schematic diagram of the experimental apparatus

the incident shock wave Mach number. In the present study, we kept the shock wave Mach number at 1.2. The internal cross-section of the test-section, which was attached to the shock tube by means of a flange, was identical to that of the shock tube. The passage of the shock wave across the first pressure transducer triggered the acquisition system and a train of laser pulses passing through the test section following an appropriate delay time. Each laser pulse produced a schlieren image on the film. In each experiment up to 40 images were captured. In all of the experiments reported here, the laser frequency was 18 kHz, i.e., 56 μs between two consecutive images. A typical schlieren image from one of the experiments is presented in Fig. 2. The complex wave pattern is clearly observed using this photography technique.

In order to insert different obstacle geometries into the shock-tube test section, a special test section was designed and built. Aligned grooves were machined on the top and the bottom walls of the test section. These grooves enabled inserting the desired obstacle geometries. The spacing between two grooves was 40 mm. Pressure transducers could be placed at different locations at the top, the bottom and at the end-walls. In most experiments, at least three pressure

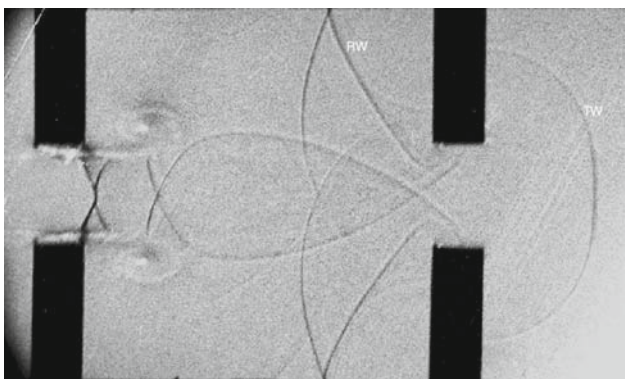

Fig. 2 A typical photograph produced by the schlieren optical system. The two 90° plates are considered as a single obstacle geometry

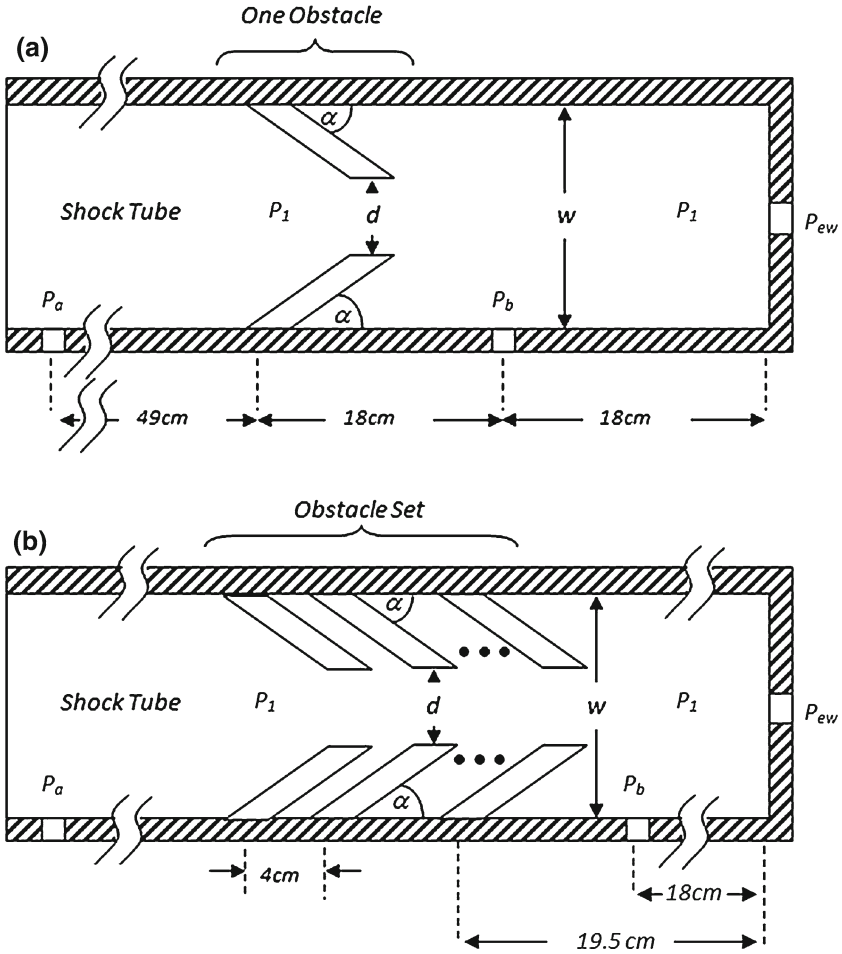

Fig. 3 The definition of relevant parameters: **a** Single-obstacle (consists of two plates); **b** multi-obstacle (consists of three single obstacles). P_a, P_b and P_{ew} are pressure transducers placed ahead and behind the overall obstacle, which can consist of one or more obstacles, and at the center of the end-wall, respectively. P_1 is the ambient pressure in the test section (1 atm). The relative opening fraction (ROF) of a single obstacle is defined as d/w. The shock propagates from left to right. The overall obstacles in this figure resemble a converging nozzle

transducers were used. An obstacle in the present notation is built from two plates erected from the top and bottom walls and inclined at different angles (the overall geometry could be symmetric or non-symmetric). The relative opening fraction (ROF), which will be used subsequently in this study, is defined as the ratio of the open size of the obstacle to the total shock tube height. Other relevant parameters related to single- and multi-obstacle geometries are defined and presented in Fig. 3a, b, respectively. A single-obstacle is built from two inclined plates with the same angle of inclination, α. The ROF is d/w (sometimes referred to by others as "porosity"). In the case of a few obstacles having different values of ROF, the ROF of the overall obstacle is defined as that of the smallest ROF of the single obstacles, i.e., $minROF_i = (d_i)/w$, where ROF_i and d_i are the ROF and the opening of the ith obstacle.

To investigate the loads developed by the shock wave after the passage of an overall obstacle geometry, two parameters were studied: the pressure at the sidewalls and center of the end-walls of the shock tube; and the reflected impulse at the center of the end-wall, that was calculated from the recorded reflected pressure. A comparison between different overall obstacle geometries was conducted to find the effect of different parameters on the shock-wave load.

Table 1 The values of the various obstacle-geometry parameters that were investigated

Relative opening fraction (ROF)	0.375	0.5	0.625		
Obstacle inclination (α)	45°	90°	135°		
Number of obstacles	1	2	3	4	5
Obstacles separation distance (mm)	40	80			

The effect of three different geometric parameters was investigated: the inclination of the plate of an obstacle, the ROF of the obstacle; and the number of identical obstacles that comprise an overall obstacle. The different experimental setup options that were investigated are shown in Table 1. Most of the experiments with each obstacle geometry were repeated at least three times in order to reduce the uncertainty. For finding the effect of the obstacles separation distance on the load that is developed on the end-wall, only the three obstacles configurations were used. To implement this experimental setup, every other groove in the test section (see Fig. 3) was used. This created an obstacles separation of 80 mm.

The total number of overall geometrical configurations that was investigated with these first three different parameters was 45 (i.e., $3 \times 3 \times 5$). Three more configurations were used to study the effect of the obstacles separation distance. In these experiments, only in the case of three obstacles, ROF = 0.375 at three different inclination angels were tested due to structure limitations of the test section. The obtained results are presented in the following.

3 Results

3.1 Single-obstacle geometry

Efforts were made to investigate the effect of different types of geometries on the load developed downstream from the overall obstacle and at the center of the end-wall. As a first step, the effect of a single obstacle was investigated. Experiments were conducted using different single symmetric obstacles with different inclinations and different ROFs. For comparison, the pressure developed downstream the obstacle was measured. Schlieren images of a typical experiment with a single obstacle inclined at 45° and ROF = 0.375 is shown in Fig. 4. The Mach number in this experiment was $M = 1.2$. The time between two consecutive images was 56 μs. The shock wave is seen, in Fig. 4a, to enter the frame from the left; the beginning of the interaction is seen in Fig. 4b. The obstacle reflects a curved shock wave upstream. When the shock reaches the opening cross-section of the obstacle, it expands and generates a vortex at the tip of each plate (Fig. 4c). The main shock that expands to the space behind the obstacle, and then propagates toward the end-wall is followed by the reflected shock waves. The generated vortex is seen to detach from the plate of the obstacle and to propagate in a curved trajectory toward the bottom/top wall (Fig. 4e). The shock-induced flow produces secondary vortices and a complex wave pattern is developed inside the gap between the overall obstacle and the end-wall (Fig. 4g–l). The reflected shock wave from the end-wall that is seen to move from right to left in Fig. 4m–p becomes curved due to the fast flow through the opening (in this case the obstacle has a general geometry of a converging nozzle).

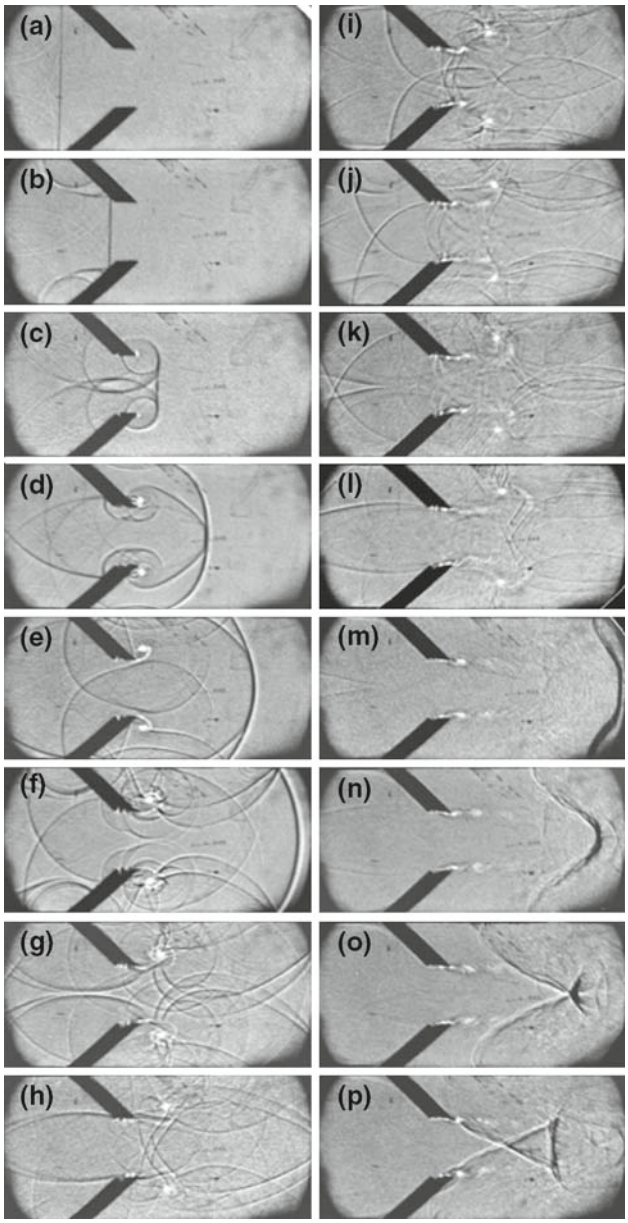

Fig. 4 Schlieren images obtained form a typical single obstacle experiment inclined at 45° and ROF = 0.375

The pressure histories measured ahead of the obstacle, P_a, behind the obstacle, P_b, and at the center of the end-wall, P_{ew}, are shown in Fig. 5. In this experiment the Mach number was $M_s = 1.196$. From 1D calculations, the incident shock-induced pressure ration is $P_{21} = 1.502$ and the overall reflected shock-induced pressure ratio is $P_{51} = 2.206$. $P_{21} = P_2/P_1$, where P_1 and P_2 are the pressures ahead of and behind the incident shock wave before interacting with the overall obstacle; and $P_{51} = P_5/P_1$, where P_5 is the pressure behind the reflected shock wave at the end-wall had it not interacted with any obstacle. The measured pressures presented, in Fig. 5, are gage pressures. As can be seen, the pressure jump measured at the gage ahead of the overall obstacle, P_a, (dotted line) agreed with our 1D-calculations. However, the pressure jumps at the gage behind the obstacle, P_b, (dashed line), and at the center of the end-wall, P_{ew}, (solid line), were somewhat lower than those obtained from 1D-calculations. Nevertheless, 6 ms after the shock reached the end-wall, the pressure developed at its center reached the 1D-predictions, namely $P_{ew} = 2.2$ atm (1.2 atm gage, where $P_1 = 1$ atm). Many reverberations of shock, compression, and rarefaction waves were observed during this time.

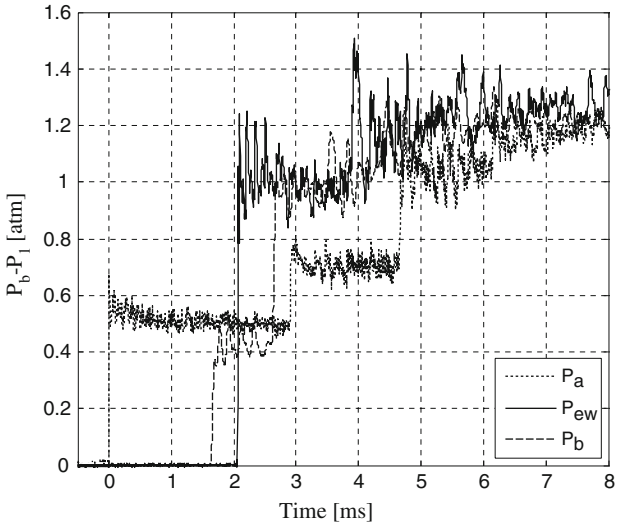

Fig. 5 Pressure histories measured by the three different pressure gages in the case of a single-obstacle inclined at 45° and ROF = 0.375

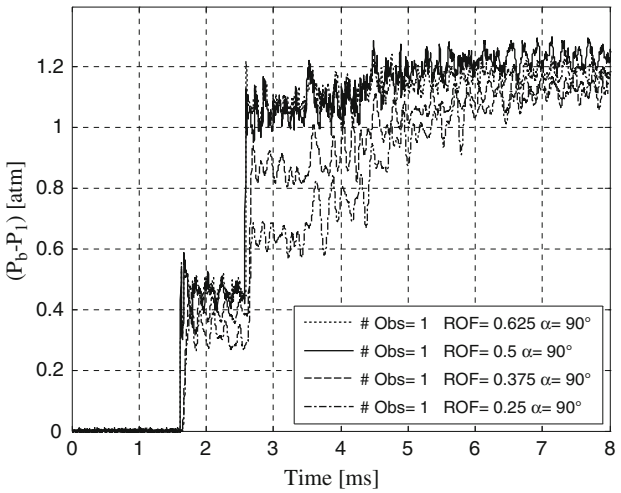

Fig. 6 Measured pressure histories of the side-wall for the case of a single-obstacle with $\alpha = 90°$ and different values of ROF. The larger is the POF the higher is pressure jump

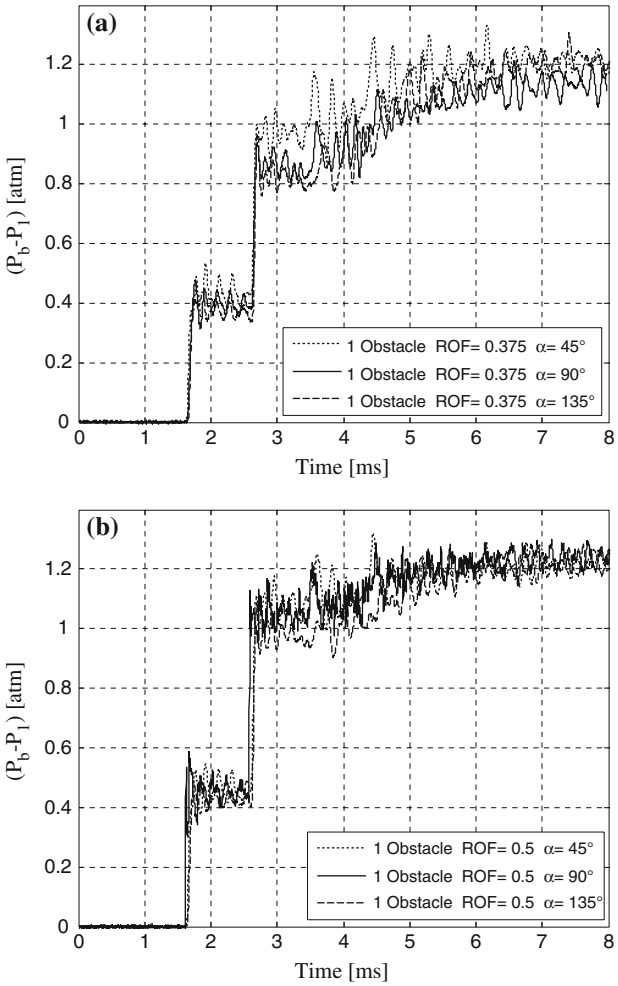

Fig. 7 Pressure histories measured at the side-wall for different inclination angles of the obstacle plate, and for: **a** ROF = 0.375, **b** ROF = 0.5

The modularity of the test section was exploited for conducting a large number of experiments with different overall obstacle geometries. The variation in the pressure jump across the transmitted shock wave was studied by varying two parameters: the ROF and the inclination of the single obstacles, α. The side-wall pressure histories for a single obstacle with $\alpha = 90°$ and four different values of ROF (0.25, 0.375, 0.50, 0.625) are presented in Fig. 6. As can be seen, the larger is the ROF the higher is the pressure jump across the transmitted and the reflected shock waves. In addition, it was found that there is a little difference between the obstacles having ROFs of 0.5 and 0.625. The pressure histories for these two obstacles were very similar and the difference between their measured reflected pressures from the 1D-calculations (without an obstacle) was only about 5% (2.1 atm as opposed to the calculated 2.2 atm without obstacles). However, keeping the ROF constant and varying the obstacle inclination angle, α, resulted in different pressure jumps. The side-wall pressure histories for inclination angles of 45°, 90° and 135° and for ROF values of 0.375 and 0.5 are plotted in Fig. 7a, b, respectively.

Figure 7a indicates that the inclination angle is significant for small values of ROF, while Fig. 7b indicates that the inclination angle has a minor effect for large values of ROF. Moreover, in both cases, after about 7 ms, the pressure at the side-wall of the test-section reached its 1D value of about $P_{51} = 2.2$.

In order to compare the obtained results to the theoretical model introduced by Britan et al. [4], the measured pressure jumps behind the transmitted shock were normalized by the pressure jump of an obstacle-free case. In this representation, the attenuation of the incident shock was observed in

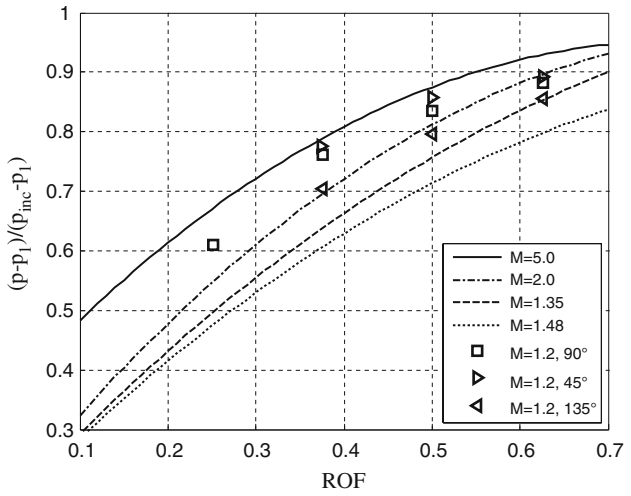

Fig. 8 The present results (*symbols*) in comparison to the model predictions (*curves*) of Britan et al. [4]

a much clearer way. As mentioned in the introduction, the model introduced by Britan et al. [4] was developed for grid-like obstacles. In Fig. 8, the results for four different incident shock wave Mach numbers are presented. The pressure attenuation as a function of ROF is seen to decrease as the ROF increased. The results of the present study are superimposed on the predictions of Britan et al.'s model [4]. The present results do not fit the model predictions in which no consideration was made to the geometry of the obstacle. Moreover, it is evident that different shock attenuations could be achieved not only for different values of ROF and different incident shock wave Mach numbers but also for different values of α. To emphasize this claim, one can see that for ROF $= 0.375$, the attenuation factor found in the present experiments, spans a range between 0.70 to 0.77, which fits the Mach number range 2–5 just by changing the inclination angle, α, while keeping a constant Mach number of 1.2.

3.2 Multi-obstacle geometry

The load on the center of the end-wall in the case of an overall obstacle that consists of more than one obstacle, i.e., multi-obstacle geometry, was also investigated. The obstacles used in the single-obstacle study were placed repeatedly as shown in Fig. 3b. Care was taken to keep the distance of the last obstacle from the end-wall constant. A set of schlieren images, as recorded for each geometry, is presented in Fig. 9. The frames in each column (I, II and III) were produced in a single experiment where the number of obstacles was 3 and their inclinations were different. In part (a) of the three cases, the shock waves are in contact with the first obstacle and the reflection waves are formed. After passing across the first obstacle, a vortex is created at the tip of each one of the two plates of the obstacle. Different vortex trajectories were observed for the different overall obstacle geometries.

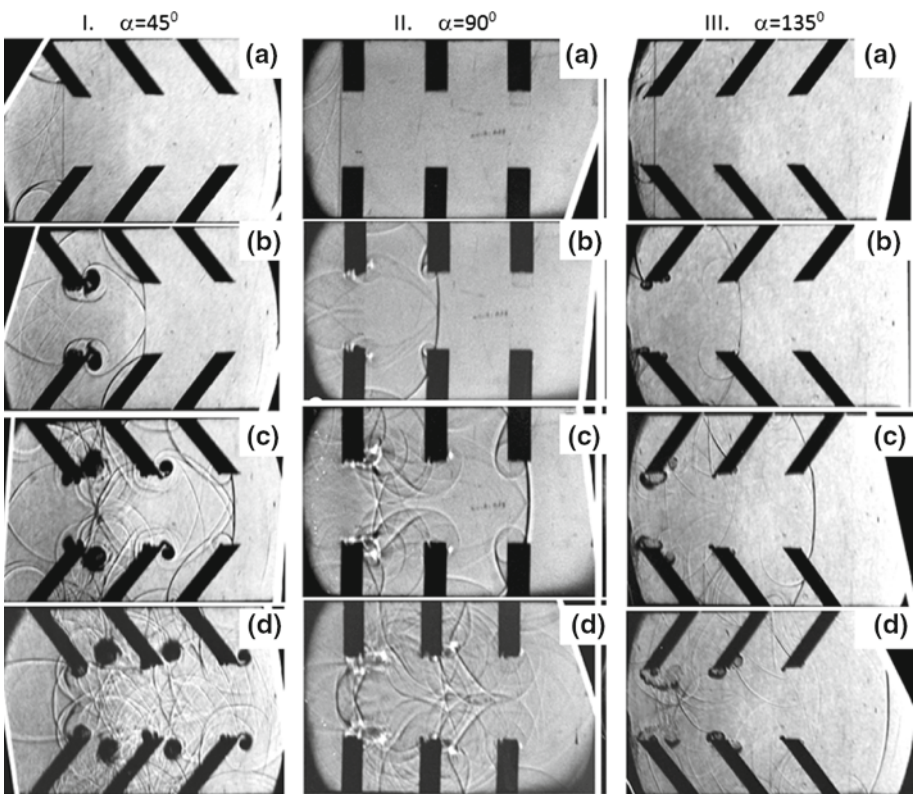

Fig. 9 Three sets of schlieren images for experiments with three different multi-obstacles. In all the images, the overall obstacle geometry is comprised of three single obstacles. The incident shock wave Mach number is $M = 1.2$, the time between two consecutive images is 0.112 ms

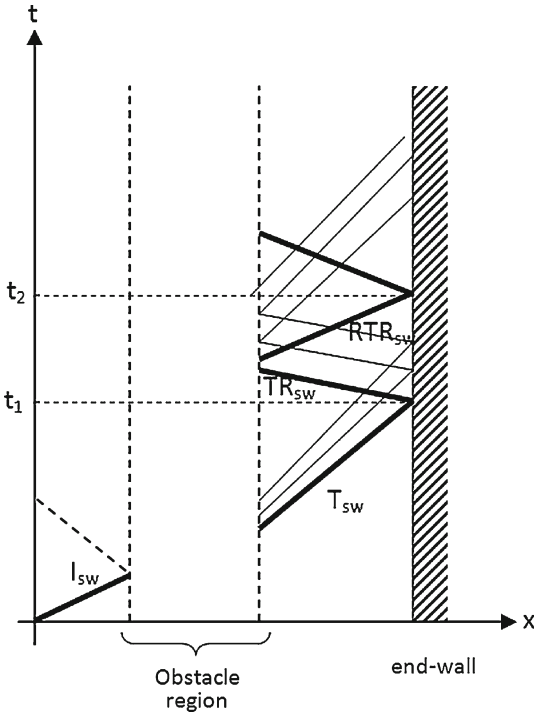

Fig. 10 Schematic (x, t)-diagram of the waves pattern. I_{sw}, incident shock wave; T_{sw}, transmitted shock wave downstream of the overall obstacle; the *thin lines* following T_{sw} represent weak waves that follow it; TR_{sw}, reflected transmitted shock wave from the end-wall; it is also followed by reflected weaker waves; RTR_{sw}, the wave reflected from the obstacle when TR_{sw} hits it; it is also followed by weaker waves; t_1, time of arrival of T_{sw} at the end-wall; t_2 the arrival time of RTR_{sw} at the end-wall

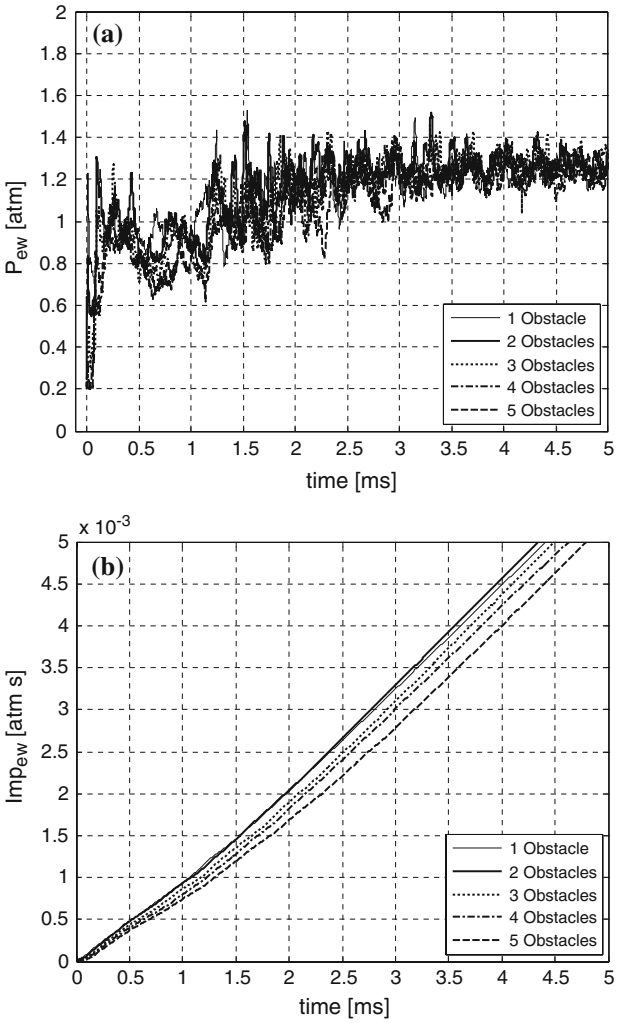

Fig. 11 **a** Pressure histories at the center of the end-wall for multi-obstacles inclined at 135°, ROF = 0.375, and 1- to 5-plate obstacles. **b** Impulses calculated from the pressure histories of part **a**. The origin of the x-axis was shifted in such a way that $t = 0$ is the time when the shock wave hits the center of the end-wall

In the 45°-obstacle geometry (Fig. 9 column I), when the shock passes each plate part of it propagates upstream (see Fig. 9b). This motion creates a strong vortex that follows the shock wave toward the bottom/top wall. Then a secondary reflected shock hits the vortex and slows its motion. This dynamics is repeated on every obstacle in the domain. In the 90°-obstacle geometry (Fig. 9 column II), similar vortex formation takes place. However, since no segments of the transmitted shock wave propagate upstream the generated vortex is less intense. In the 135°-obstacle geometry (Fig. 9 column III), the vortex that is generated by the shock wave is the weakest. In this obstacle geometry the plates "chop" the shock wave, the central part of it expands while the two other (chopped) parts are trapped in the space between the plates and the bottom/top wall and do not propagate towards the end-wall. The vortices in this case move with curved trajectories from the tip of the plates toward the center and then back toward the bottom/top wall.

It is also interesting to note that in the 45°-obstacle geometry case, the wave patterns that are visible are much more complex than those of the 90°-obstacle geometry case. This complexity of the 45°-obstacle geometry case is even more prominent with respect to the 135°-obstacle geometry case.

In order to understand the complexity of the pattern of the waves that is developed as a result of the interaction between the incident shock wave and the overall obstacle, an illustrative schematic (x, t)-diagram is presented in Fig. 10. Isw indicates the incident shock wave that interacts with the obstacle, Tsw is the transmitted shock wave downstream of the overall obstacle, t_1 is the time of arrival of Tsw at the end-wall. The thin lines following Tsw represent the weak waves that follow it. TRsw is the reflected transmitted shock wave from the end-wall. It is also followed by weaker reflected waves. RTRsw is the wave reflected by the plates of the last obstacle when TRsw hits it. It is also followed by weaker waves, t_2 is the arrival time of RTRsw at the end-wall.

The pressures that are developed at the center of the end-wall for 1–5 plate obstacles with ROF = 0.375 that are inclined at 135° are shown in Fig. 11a. It is evident that

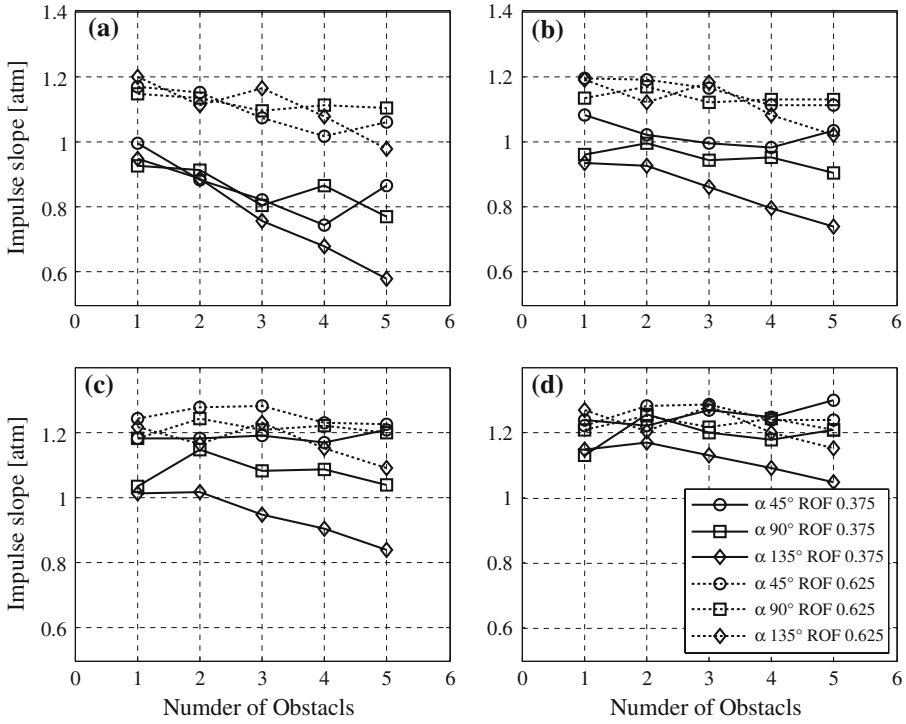

Fig. 12 Impulse linear slopes for two different ROFs (0.375 and 0.625), different inclination angles (45°, 90° and 135°), and different number of obstacles (1–5). **a** Integration time $t_c = 0.25$ ms. **b** Integration time $t_c = 1$ ms. **c** Integration time $t_c = 2$ ms. **d** Integration time $t_c = 5$ ms

the number of obstacles affects the pressure history at the end-wall.

A single parameter that represents the load for the different setups is needed in order to conduct a comparison between the different obstacle geometries. It was found that the impulse linear slope that is developed at the center of the end-wall is an appropriate parameter for comparing between the different obstacle geometries. To find the impulse linear slope, one has to calculate the time integral of the pressure that is measured at the center of the end-wall, P_{ew}:

$$I(t_c) = \int_{t_0}^{t_c} P_{ew}(t')\mathrm{d}t' \tag{1}$$

where t_0 is the time when the incident shock reached the end-wall. As can be seen from Eq. (1) the impulse depends on the chosen value of the upper limit of the integral, t_c, namely; the impulse integration time. The impulse linear slope was obtained by calculating the ratio $I(t_c)/(t_c - t_0)$.It should be noted that the dimension of the impulse linear slope is pressure (atm in the present case). The impulses for overall obstacles with 1–5 obstacles for the case of 135° inclination and ROF = 0.375 are plotted in Fig. 11b. The origin of the x-axis in the graph was shifted in such a way that $t = 0$ is the time when the shock wave hits the center of the end-wall. The different impulses and consequently the different impulse linear slopes that were developed at the center of the end-wall were calculated using different experimental setups with different ROFs, different number of obstacles and different angles, α.

The comparison between the different obstacle geometries is shown in Fig. 12. Two different ROFs are presented for different inclination angles and different number of obstacles. The impulse linear slope where the impulse integration time, t_c, was 0.25 ms is presented in Fig. 12a. The different impulse linear slopes that were developed at the center of the end-wall became significant at early time. In this case, only the incident shock wave and some weak shock waves that were generated by the obstacles and followed it had contributed to the impulse as can be seen from the (x, t)-diagram shown in Fig. 10 as T_{sw}. A distinct behavior is seen between the ROFs cases. It is evident from Fig. 12a that up to $t_c = 0.25$ ms increasing the number of obstacles to two ROF geometries reduced the load developed at the center of the end-wall and that the shock-wave load was attenuated more effectively by the diverging nozzle geometry, namely for inclination angle of 135°. The little difference between the loads developed at the end-wall with respect to the different inclinations angles indicates that up to this time, the effect of the geometry is minor.

When the impulse integration time was $t_c = 1$ ms, the linear impulse slope at the center of the end-wall, as shown in Fig. 12b, had the same typical behavior that was shown in Fig. 12a, namely a reduction, although less significant, in the shock wave load while increasing the number of the obstacles. However, the effect of the obstacle geometry was more pronounced in the ROF = 0.375 case than in the

ROF = 0.625 case. Figure 12c, d present the impulse linear slope up to integration times $t_c = 2$ ms and $t_c = 5$ ms, respectively. At these times, the reflected waves from the last obstacle (RTR_{sw} in Fig. 10) had reached the end-wall and increased the load. It is interesting to note that there is an increase in the impulse linear slope when increasing the number of obstacles in the ROF = 0.375, $\alpha = 45°$ case. On the other hand, there is a decrease in the impulse linear slope when increasing the number of obstacles in the ROF = 0.375, $\alpha = 135°$ case. This effect becomes more dramatic for the 5 ms integration time. The different trends between the short integrating time in which the impulse linear slopes decrease while increasing the number of obstacles (Fig. 12a) and the mixed trend (increasing or decreasing) for the long integration time (Fig. 12d) can be explained as follows: in the short integration time, the impulse calculated is affected mainly by the incident shock wave and not by the reverberations of the reflected shocks between the back end of the overall obstacle and the end-wall. In this case, each obstacle that the shock passes, reflects part of it. Therefore, at a short integrating time, the attenuation of the shock wave increases when the number of the obstacles is increased. This process attenuates the shock strength reaching the end-wall while increasing the number obstacles. The efficiency of the attenuation depends on the obstacle geometry. On the other hand, when calculating the impulse using longer integration times, the reverberation between the back end of the overall obstacle and the end-wall are accounted for and in this case two effects play a major roll: the efficiency of the obstacle to reflect upstream the incident shock wave and the efficiency of the obstacle to trap the shock wave between it and the end-wall. This, in turn, depends on the geometry and in this case different trends were observed. According to this interpretation, from Fig. 12a and d it is seen that for $\alpha = 135°$ and ROF = 0.375 the incident shock wave that reached the end-wall was attenuated most effectively while increasing the number of obstacles. These results suggest that a diverging geometry is more efficient for reflecting waves than other geometries. The same argument holds for the reflected shock wave from the end-wall. In the case of $\alpha = 135°$, the reflection efficiency is the lowest (the reflected shock wave travels up-stream) and the reflected shock wave passes through the obstacles with little attenuation. This mean that the shock wave trapped between the back end of the obstacle and the end-wall is the weakest with respect to the other geometries.

Since the impulse linear slope has a unit of pressure, it can be considered as the effective pressure at the center of the end-wall as a result of the entire interaction, In turn, this effective pressure could be considered as a result of an effective shock wave that reflects head-on from the end-wall without passing through any obstacle. In the case of no obstacles, the impulse linear slope is identical to the pressure jump at the end-wall. In the present study, the incident Mach number that was used in all the experiments was 1.2 under ambient conditions, which leads to pressure jump of 1.2 atm on the end-wall, i.e., $P_{51} = 2.2$. Taking this value as a reference point, it is evident that in some cases the end-wall experienced pressure amplifications while in others, pressure attenuations. It is interesting to note that the same impulse linear slope could be reached by different values of ROF and different angle inclinations especially when increasing the number of the obstacles. This behavior suggests that the obstacle geometry becomes increasingly important while increasing the number of obstacles. A common observation that is clear from Fig. 12a–d is that the geometry effect plays an important role for small ROF. The scattering of the measured load in the ROF = 0.625 case are significantly lower than in the ROF = 0.375 configurations.

In order to investigate the effect of the separation distance between the obstacles on the load developed on the center of the end-wall, a set of experiments was done in which three obstacles were positioned in the test section. The test section limits the separation distance between the obstacles to 40 and 80 mm for the short separation distance and long separation distance, respectively. The ROF was 0.375 for all the separation distances, since for this value the effect of the obstacles on the load developed at the center of the end-wall is most dramatic. The inclination angles were 45°, 90° and 135°. The distance between the last obstacle to the end-wall was kept constant. The impulses developed at the center of the end-wall are shown in Fig. 13a. The thin lines are for the short separation distances, and the full, dotted and dashed lines are for the different inclination angels 45°, 90° and 135°, respectively. It is clear that the impulse developed on the center of the end-wall decreases while increasing the obstacles separation distance, and as found earlier, the diverging inclination angle attenuates the shock load at the center of the end-wall more effectively. The impulse slope calculated versus four different integration times using the impulses presented in Fig. 13a are shown in Fig. 13b. The same overall behavior found in Fig. 12a–d are seen for this case, i.e., the load attenuation effect decreases when the integration time is increased, and diverging type obstacles configurations attenuate the load more effectively. However, in all the configuration pairs (having the same inclination angle) that were tested in this set, the loads developed at the center of the end-wall are lower in the long distance separation cases than those developed in the short distance separation cases.

However, as seen in Fig. 13b for $\alpha = 135°$ and $d = 40$ mm and $\alpha = 90°$ and $d = 80$ mm, we found that the inclination angle and the obstacles separation distance parameters can compensate each other for integration times longer than 1 ms. From this set of experiments we found that the shock load developed at the center of the end-wall decreases by increasing the obstacles separation distance, which increases the volume for the shock wave to expand to.

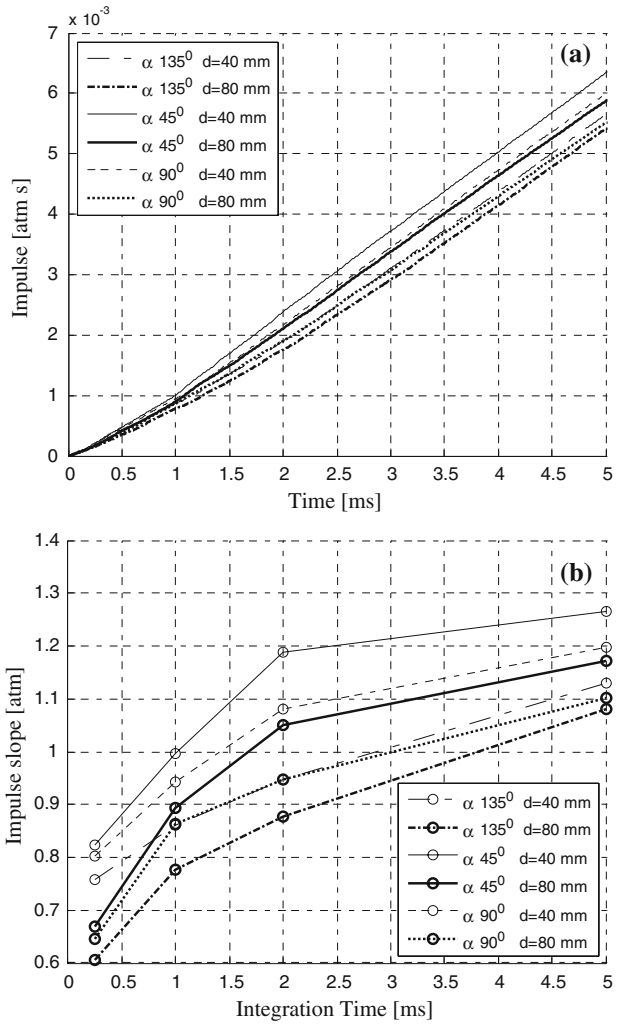

Fig. 13 **a** Impulse calculated for two different obstacle separation distances, $d = 40$ mm (*thin line*), $d = 80$ mm (*thick line*), in the three-obstacle case using ROF $= 0.375$ and $\alpha = 45°$, 90° and 135° (*full line*, *dashed line* and *dotted line*, respectively). **b** The impulse slope calculated up to four different integration times from the impulses presented in **a**

4 Conclusions

The effect of different types of obstacles on the load developed by a shock wave was investigated. Focus was given to the effect of the obstacle geometry and the number of obstacles that comprise the overall obstacle. In the case of a single obstacle, the ROF played, as expected, a major role on the shock-wave load attenuation. The larger was the ROF the greater was the effect of the geometry on the shock-wave load. It was found that the pressure behind the shock wave that was developed in diverging nozzle-like obstacles was lower than that developed in converging nozzle-like obstacles even when the ROFs were the same. The results from the single obstacle study were compared to the 1D model introduced by Britan et al. [4] and a discrepancy was found. This was attributed to the fact that unlike the present case, in Britan et al.'s model, which was developed for grid-like obstacles with small openings, the flow could be choked.

In the case of multi-obstacle geometries, the load on the center of the end-wall was found to decrease when increasing the number of obstacles at early time when the reflections of waves from the end-wall did not reach the end-wall. Later, amplification and attenuation effects were observed when increasing the number of obstacles. Once the transmitted shock wave reached the end-wall, it was reflected back towards the overall obstacle. This initiated multiple reflections between the overall obstacle and the end-wall. On one hand, the obstacle prevented shock wave propagation toward the target end-wall and reduced its intensity, on the other hand, the same obstacle prevented the reflected shock wave from leaving the end-wall region, and the load increased on the end-wall by the reverberation of the shock waves between the end-wall and the obstacle. In this case, the obstacle geometry played an important role. The obstacle geometry should prevent the waves from passing through it toward the end-wall (target) but enable passage of the reflected shock waves upstream away from the end-wall with as little interference as possible. For this reason divergent-nozzle like geometries are superb.

While the ROF was found to be the dominant parameter in all the experiments, the geometry was the second most significant parameter in attenuating/amplifying the shock-wave loads that were developed on the end-wall. However, in some cases those parameters could compensate each other as was presented in Fig. 12d, where it can be seen that the load at the end-wall for four obstacles with $\alpha = 90°$ and ROF $= 0.625$ is similar to that of four obstacles $\alpha = 45°$ and ROF $= 0.375$. Increasing the number of obstacles could cause, in some cases, load amplification, which arose from the waves that reflected back and force between the end-wall and the overall obstacle. Hence, overall obstacles could either attenuate or amplify the shock-wave load.

When the shock wave crosses an obstacle it expands to the volume down stream. Increasing the volume by increasing the separation distance between the obstacles decreases the shock load developed at the center of the end-wall.

Understanding the complex wave dynamics and the flow patterns is crucial for designing suitable shock attenuators or shock amplifiers.

Acknowledgments The authors would like to acknowledge the useful technical assistance of Mr. D. Hirshler. This research was partly supported by the Israeli MoD.

References

1. Dosanjh, D.S.: Interaction of grids with traveling shock waves. NACA TN 3680 (1956)

2. Lind, C., Cybyk, B.Z., Boris, J.P.: Attenuation of shock: high Reynolds number porous flow. In: Ball, G.J., Hiller, R., Roberts, G.T. (eds.) Proceedings of 22nd International Symposium Shock Waves, Imperial College, London, UK, pp. 1138–1140 (1999)
3. Franks, W.J.: Interaction of a shock wave with a wire screen. UTIA TN, 13 (1957)
4. Britan, A., Igra, O., Ben-Dor, G., Shapiro, H.: Shock wave attenuation by grids and orifice plates. J. Shock Waves **16**(1), 1–15 (2006)
5. Igra, O., Wu, X., Falcovitz, J., Meguro, T., Takayama, K.: Experimental and theoretical study of shock wave propagation through double-bend ducts. J. Fluid Mech. **437**, 255–282 (2001)
6. Elperin, T., Ben-Dor, G., Igra, O.: Head-on collision of normal shock waves in dusty gases. Int. J. Heat Fluid Flow **8**(4), 303–308 (1987)
7. Igra, O., Elperin, T., Ben-Dor, G.: Blast waves in dusty gases. Proc. R. Soc. Lond. A **414**, 197–219 (1987)
8. Igra, O., Wu, X., Hu, G.Q., Falcovitz, J.: Shock wave propagation into a dust-gas suspension inside a double-bend conduit. J. Fluids Eng. **124**, 483–491 (2002)
9. Sasoh, A., Matsuoka, K., Nakashio, K., Timofeev, E., Takayama, K., Voinovich, P., Saito, T., Hirano, S., Ono, S.: Attenuation of weak shock waves along pseudo-perforated walls. J. Shock Waves **8**(3), 149–159 (1998)
10. Britan, A.B., Zinovik, I.N., Levin, V.A.: Measurement of parameters of a gas suspension behind a shock wave in foam. Fluid Dyn. **28**(3), 400–405 (1993)
11. Kitagawa, K., Yasuhara, M., Takayama, K.: Attenuation of shock waves propagating in polyurethane foams. J. Shock Waves **15**(6), 437–445 (2006)
12. Sadot, O., Anteby, I., Harush, S., Levintant, O., Nizri, E., Ostraich, O., Schenker, A., Gal, E., Kivity, E., Ben-Dor, G.: Experimental Investigation of dynamic properties of aluminum foams. J. Struct. Eng. **131**, 1226–1232 (2005)
13. Schardin, H., Reichenbach, H.: The behavior of shock waves in ducts and when entering entrance structures. In: Proceedings of Symposium Protective Structures for Civilian Populations, National Research Council (USA) Washington, DC, USA, pp. 193–206 (1965)
14. Abe, A., Takayama, K.: Attenuation of shock waves propagating over arrayed spheres. In: Takayama, K., Saito, T., Kleine, H., Timofeev, E. (eds.) Proceedings of 24th International Congress High-Speed Photography and Photonic, Sendai, Japan: SPIE The international Society for Optical Engineering, pp. 582–588 (2000)